2-3 Solar Wind Plasma Instrument for the L5 mission

MIYAKE Wataru and KAZAMA Youichi

The objectives of the solar wind plasma instrument for the L5 mission are to forecast the geomagnetic storms by means of the measurement of solar wind parameters for identifying the disturbances, and to study the particle acceleration processes, wave-particle interactions and propagation of accelerated particles in the interplanetary space. The instrument has a set of electrostatic deflectors for 2π str field of view and a spherical electrostatic analyzer. We developed a numerical model to obtain the energy-angle characteristics and the geometrical factor of the instrument. We conclude that the instrument under consideration is suitable for the solar wind plasma measurement.

Keywords
L5 mission, Solar wind plasma, Electrostatic analyzer

1 Introduction

The L5 point, located 60° east of the Sun, is considered one of several locations in which a steady space-weather monitoring satellite may suitably be deployed in the future[1]. Consideration is now being given to the inclusion of a solar wind plasma instrument, in addition to CME (Coronal Mass Ejection) imaging equipment and the like, among the equipment on board such an L5 fixed-point solar observation satellite. This paper introduces the results to date of a conceptual study on this plasma instrument.

2 Objectives of Solar Wind Plasma Observation

2.1 Factors of Geomagnetic Disturbances

The solar plasma is an energy source that fills the interplanetary space between the Sun and the Earth, forming the magnetosphere by confining the geomagnetic field, and governing the activities of the magnetosphere. Therefore, variation in the solar wind is of fundamental importance in predicting disturbances inside the magnetosphere, including geomagnetic storms. Two major factors relating to the solar wind are known to affect geomagnetic storms; namely, CMEs and high-speed solar winds from coronal holes[2]. Monitoring and tracing of CMEs projected toward the Earth is the main objective of the L5 mission; this is to be achieved by observations with imaging devices capable of a wide viewing range[1].

The main objective of a solar wind plasma instrument placed at the L5 point would be to perform routine preliminary monitoring of the high-speed solar wind (Fig.1). It is hoped that observation at the L5 point will enable us to

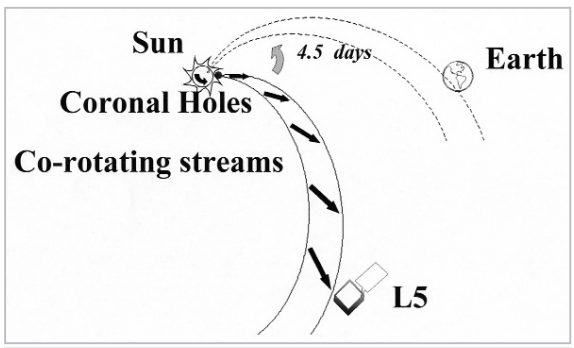

Fig.1 *A conceptual diagram of high-speed solar wind preliminary monitoring at the L5 point*

understand the characteristics and structure of the solar wind approximately four days prior to the date at which the solar wind will affect the Earth, leading to dramatically improved precision in space weather forecasting, which is currently based on coronal-hole and solar-wind observation data gathered from the position of the Earth's orbit; analysis of this data takes places when the data is 27 days old and relies on the recurrent nature of the phenomena involved.

Moreover, solar wind plasma observation at the L5 point will offer valuable data that will help us to grasp the background solar wind structure; this will prove essential in modeling the propagation to the Earth of shocks and disturbances and in predicting the propagation of high-energy particles. The solar wind measured at the L5 point as time series data can be analyzed to determine the solar wind structure between the Sun and the Earth, excluding sudden disturbances (such as CMEs) that propagate through this solar wind structure to arrive at the Earth. In addition to the interpretation of the solar wind observation data at one point in situ, the observation of the non-thermal component of electrons can be applied to the detection and identification of the interplanetary magnetic field (IMF) structure connected on the Sun[3][4]; such observation, combined with magnetic field observation in the vicinity of the Earth and at the L5 point, permits us to infer the structure of the solar wind.

The shock and disturbance accompanying a CME propagate to arrive at the Earth's orbit, at the same time interacting with the preceding solar wind. For example, it is known that this interaction reduces the velocity of the shock during its flight from the vicinity of the Sun to its arrival at the Earth's orbit[5]. Moreover, it is known from comparison between the velocity of the CME observed in the vicinity of the Sun and the velocity of the solar wind in the CME in the vicinity of the Earth that assimilation of the velocity of the CME into the velocity of the background proceeds as a result of interaction between the CME and the background solar wind[6]. To model the propagation of the disturbance and to predict the time of arrival at the Earth, it is essential to grasp the structure of the background solar wind between the Sun and the Earth; accordingly, observation of the solar wind plasma at the L5 point is extremely important.

Moreover, as a result of this interaction, the preceding background solar wind is compressed in front of the CME and a sheath region is formed between the shock and the CME. It is known that this sheath region, together with the main part of the CME that follows, gives rise to geomagnetic storms[7], and that the characteristics of this region play a significant role in storm development, particularly in cases of large geomagnetic storms[2]. This provides further indication of the importance of understanding the background solar wind structure preceding CMEs.

2.2 High-energy Particle Acceleration

The shock in the solar wind and a co-rotating interaction region (CIR) are also important targets of observation, as sources of high-energy particles[8] in interplanetary space. The solar wind plasma also plays a role as a source of particles that will be accelerated to become high-energy particles. The observation of the non-thermal component in the solar wind plasma is important in order to determine the efficiency of acceleration of particles by the shock, as the energy in such acceleration serves as a threshold; only particles whose energies exceed a given energy before being injected into the shock can be accelerated effectively. The existence of the non-thermal velocity distribution component has been clarified through recent observations of the solar wind plasma by the ACE, WIND, and Ulysses satellites[9]-[11], indicating ion acceleration of up to approximately 0.1 MeV, which acceleration is not due to the shock. However, the details of this acceleration remain unknown.

These non-thermal components also include pickup ions originating both in interstellar space and within the solar system, and hence observations in this case are quite sig-

nificant. Among neutral particles in interstellar space, only He, with a high ionization potential, can enter into a 1 AU region. Variation of He^+ within the internal solar system should depend on solar activity, but the task of elucidation of the details of this variation remains for the future. Further, trace amounts of pickup ions have been observed that cannot be explained as originating from interstellar space, such as S^+ and C^+. A theory proposing the internal solar system as the origin of dust has been put forward[12], but elucidation of this problem also remains for the future. It is thought that these pickup ions are accelerated by the shock at the end of the heliosphere to become anomalous components of cosmic rays, arriving at the inside of the internal heliosphere again[13]. However, the mechanism of acceleration and generation remains unexplained within such a scenario. Thus pickup ions are significant targets of observation.

The energy range of the heavy ions and the non-thermal ions in the solar wind corresponds to the lowest edge of the spectrum of the high-energy particles generated by the shock and CIR. With the data for heavy ions and non-thermal ions combined with the data from the high-energy particle measuring instrument, a whole spectrum of accelerated particles will be available, contributing to the elucidation of the mechanism of high-energy particle acceleration in the shock and CIR.

2.3 Source Region of Solar Wind

The ion composition and ionization state in the solar wind plasma carry important information about the origin of the solar wind plasma in the solar corona[14]. The ionization state is also referred to as a "thermometer" of the corona, which is the source of the solar wind. After the solar wind leaves the corona, the plasma is almost collisionless, and processes of ionization, recombination, and the like do not proceed further; therefore, ionization is "frozen" in the state seen in the corona. Further, it is known that there are clear differences in composition between low-speed and high-speed solar winds emanating from the coronal hole, reflecting differences in the state of the corona generating these winds. In particular, peculiar ion compositions and ionization states observed at the time of disturbances[15][16] (such as CMEs) provide important data in the determination of the emission region in the lower coronal region and help provide an understanding of the physical mechanism in question. Moreover, anomalous increases of heavy ions and observation of the ionization states thereof are also used to identify regions of emission of matter from the Sun, including CMEs, and hence this can be said to comprise essential data in research into the large-scale structure of solar wind disturbances. The compositions and ionization states of the ions in the solar wind provide valuable verification data with respect to the mechanism of acceleration and transportation of high-energy particles, through comparison with the compositions and ionization states of the high-energy particles accelerated by the shock.

The non-thermal electron flow (referred to as the "halo" or "strahl") in the solar wind plasma is important in tracing the magnetic field lines in interplanetary space, due to the motion of this flow along the magnetic field lines[3][4]. From the bi-directional non-thermal electron distribution, a closed magnetic field structure having its root on the Sun may be inferred[17]. Moreover, from observation of the electron flow accompanying an impulsive flare, linkage of the magnetic field lines with a corresponding region on the solar disk is suggested[18]. This enables us to make a number of inferences concerning the source of the solar wind, and to draw conclusions concerning solar emissions (such as a magnetic clouds), ejected structures, and propagation characteristics.

2.4 Relationship with Wave Phenomena

Type Ⅱ solar radio burst has become an important index of the generation of solar wind disturbance and provides evidence of shock generation. Similarly, type Ⅱ solar radio burst in the km waveband, which cannot be observed on the ground due to the ionosphere,

is believed to be emitted by electrons accelerated by the interplanetary shock, and thus such radio burst forms an important observation target for the plasma wave receiver in the L5 mission. The observation of non-thermal electrons is important in order to verify the mechanism of this radiation of electromagnetic waves and to determine the validity of (and limits to) the use of such observation in monitoring shock in cases of type Ⅱ radio burst. Moreover, type Ⅲ radio burst in interplanetary space is considered to be generated by the electron flow accompanying an impulsive flare[19]. The observation of such radio burst also contributes to research into the mechanism of electromagnetic-wave emission from the electron flow. Information concerning the electron distribution function is required in understanding plasma wave phenomena (such as the Langmuir wave and the whistler mode wave in the solar wind) and wave-particle interaction. Among these phenomena the whistler mode wave in particular is considered important in electron acceleration within the shock, in that it plays the same role as an MHD wave in ion acceleration, serving as a reflector and a trapper. However, observation of this phenomenon has been limited[20], and thus quantitative evaluation remains a task for the future.

Further, the MHD waves in the solar wind are identified from magnetic field data and ion observation data. It is thought that in the particle acceleration caused by the shock, acceleration progresses to higher energy through the process of wave excitation by the accelerated particle itself and through scattering and acquisition of particles by that wave[8]. Moreover, it is considered that the wave also takes part in ion acceleration (up to approximately 0.1 MeV) that is not due to the shock; this concept and the mechanism involved have recently drawn attention as meriting further study.

3 Characteristics of Solar Wind Plasma

3.1 Thermal Proton

Measurement of the thermal proton is indispensable in calculating bulk velocity, density, and temperature, all of which are basic macro parameters of the solar wind. Using these basic parameters, the shock and disturbance resulting from the CME in the solar wind, the CIR, and the high-speed solar wind are detected and identified. Moreover, variations in these basic parameters are used together with the magnetic field data to detect and identify the MHD wave in the solar wind, providing basic information concerning pitch angle scattering, heating, and acceleration of ions.

The energy versus arrival-direction distribution of ions in the solar wind is shown in Fig.2[21]. The direction of the Sun is set to 0° in the figure and the distribution indicates angle distribution in the ecliptic plane. Solar wind proton flow is a supersonic flow with large particle counts, and hence is said to be an easy target for measurement given the sensitivity of current equipment. On the other hand, the thermal velocity (a few tens of km/sec) is low relative to the bulk velocity (a few hundreds of km/sec). In order to acquire the detailed energy-angle distributions necessary to obtain the velocity distribution function, higher energy resolution and angle resolution are required relative to ion measurement in the magnetosphere.

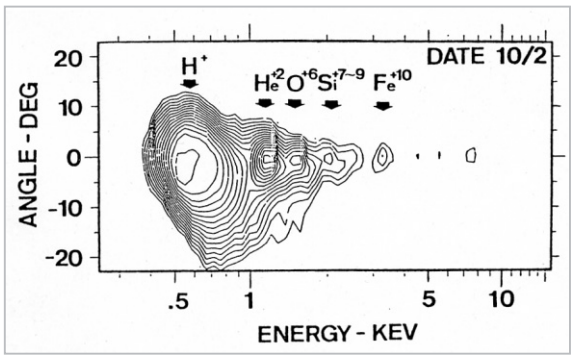

Fig.2 *Typical energy-angle distribution of solar wind ions*

3.2 Heavy ions and non-thermal velocity distribution

The peak seen at 1 keV or higher in Fig.2

represents heavy ions in the solar wind. Since protons and heavy ions have nearly the same velocity in the solar wind, observation with this E/q analyzer yields a distribution that reflects the M/q ion values. That is, the distribution of He^{++} features a peak at an energy level almost twice that of protons (H^{+}). Heavy ions in the solar wind are of particular importance in two ways; first, they serve as a source of high-energy particles that are generated and accelerated by the interplanetary space shock, and second, their composition and ionization state provide clues as to the origin of CMEs and the like within the solar corona. Observations are also being performed by currently active satellites in the vicinity of the Earth, such as the ACE and WIND satellites, and these observations will prove valuable in solar-wind plasma observations conducted in the context of the future satellite programs of various foreign countries.

The most significant heavy ion in the solar wind is He^{++} (α particle); its density is 20% or less of that of the solar wind proton[22]; other heavy ions have even smaller densities. For this reason, to date three-dimensional velocity distribution functions have been obtained only for protons and He^{++}; for other heavy ions, only energy distributions (obtained by integrating incoming-angle directions) have been obtained[11].

3.3 Thermal electrons and non-thermal electrons

These electrons are important in determining the large-scale magnetic field structure of interplanetary space. Moreover, their velocity distribution functions are required for interpretation of plasma wave phenomena in the solar wind. Furthermore, observation of these electrons also contributes to elucidation of particle acceleration mechanisms in the impulsive flare and in the shock. Generally, the electrons of the solar wind form an isotropic thermal core whose energy ranges up to about 30 eV and a halo consisting of a high-energy tail that extends along the magnetic field lines up to a few hundreds of eV[23]. Furthermore, electrons accelerated by a flare or the like propagate with energies of hundreds of eV or more, mainly in the direction of the magnetic field lines[18].

Characteristics of the above-mentioned observation targets are summarized in Table 1 below.

4 Analyzer Numerical Model

4.1 Outlines of Instruments

As for instruments intended mainly for, or designed in consideration of, observation of the solar wind plasma, up to now there have been three examples developed in Japan and carried aboard satellites; for two of these instruments, 270° spherical electrostatic analyzers[21][24] were used, while in the third a top-hat type electrostatic analyzer[25] was employed. However, all of these satellites relied on spin stabilization attitude control. Each of the above-mentioned instruments thus featured one-dimensional angle resolution, and was positioned in the satellite in such a way that the one-dimensional field of view lay on the plane containing the spin axis of the satellite. The combination of the spin of the satellite and this one-dimensional angle reso-

Table 1 *Characteristics of main observation targets*

	Thermal protons	Heavy & non-thermal ions	Thermal & non-thermal electrons
E／Q	0.4—3keV/q	0.8—60keV/q	thermal : —50eV/q non-thermal : 50eV-tens of keV/q
M／Q	1	2—8	—
Flux	$\sim 10^{8}$/cm^{2}s str eV	$<10^{7}$/cm^{2}s str eV	$<10^{7}$/cm^{2}s str eV
Angular distribution	± 10° from the sun	heavy : ± 5° from the sun non-thermal : unknown	Solar wind electrons : all directions Flare electrons : ± 30° from the magnetic field line

lution enables measurement of angle distributions of two orthogonal components, which are used together with measurement of the energy distribution to obtain a three-dimensional velocity distribution function.

An ion sensor of the L5 mission is assumed to cover a measurement E/Q range of 0.3−60 keV/q and an M/Q range of 1−10 as targets. In order to separate multiply-charged heavy ions in the solar wind from the high-energy tail (composed of protons and α particles) and thus render observation possible, the ion sensor is designed as a combination of two analyzers: an electrostatic analyzer to analyze [energy]/[electric charge] (E/Q), and a TOF (Time-Of-Flight) analyzer to analyze velocity. Moreover, since the satellite is oriented for imaging system missions and three-axis control is assumed, the sensor obtains angle distributions by sweeping its field-of-view direction electrostatically. This represents a difference from the analyzers aboard conventional Japanese satellites.

A schematic diagram of the ion sensor is shown in Fig.3 The ions in the solar wind are first subject to selection, based on incidence direction, in the field-of-view sweeper portion of a trumpet-like structure on the upper portion of the sensor. The ions that have passed through this structure then pass through sensitivity adjustment electrodes that enable observation of both thermal protons and heavy ions (in addition to non-thermal components), although the absolute quantities of these particles differ greatly, then passed through a flux "diaphragm" to be concentrated in a narrow beam. The ions are then subjected to E/Q selection by the spherical electrostatic analyzer and further subjected to TOF analysis using a thin sheet of carbon foil. This TOF analysis measures, for an electron emitted by an ion, the time between its passage through the thin foil and its arrival at the detector. For the particle detector, multi-anode MCP capable of detecting a one-dimensional position is used, and the angle distribution of the ions is determined in a two-dimensional plane using the obtained positions together with field-of-view sweeping. In particular, since the ion distribution is concentrated in the solar direction, the anode corresponding to the solar direction features fine divisions.

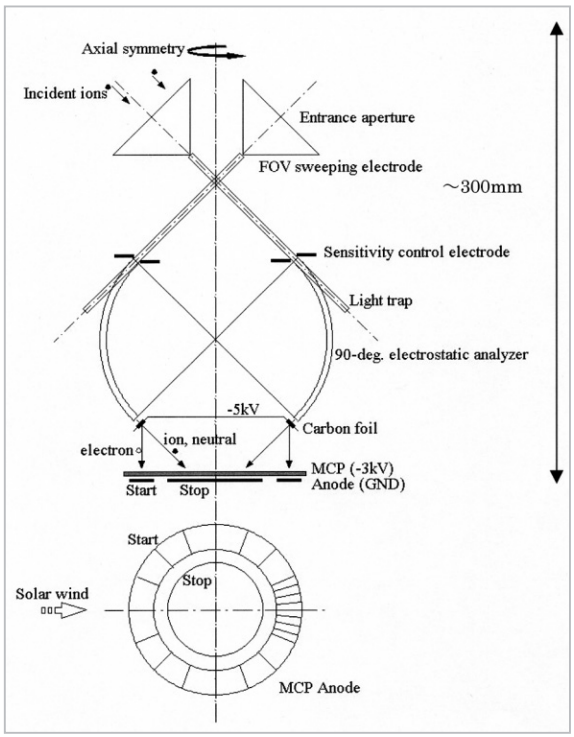

Fig.3 *Schematic diagram of ion sensor*

The measurement energy range of an electron sensor is assumed to be 0.02−20 keV/q. The electron sensor is essentially configured of an ion sensor without the M/Q TOF analyzer (downstream from the carbon foil) or the sensitivity adjusting electrodes. As electrons have a wide angle distribution, it is necessary to measure the entire field of view in order to detect the non-thermal component, which is bi-directional with respect to the magnetic field lines. Therefore, it is preferable to ensure a complete field of view with two onboard sensors.

4.2 Numerical Model of Electrostatic Analyzer

By analyzing in detail particle movement in the sensor (as shown in Fig.3), it becomes possible to evaluate whether or not sensor performance−in terms of sensitivity, measurement energy range and resolution, field-of-

view range, and angle resolution—is sufficient for the measurement of solar wind plasma. In the present case, we established a numerical model for a common component of both the ion sensor and the electron sensor, which model extends as far as the output of the spherical electrostatic analyzer; we then examined the performance of the model as an E/Q analyzer by applying electric potentials to the electrodes, finding a spatial electrostatic field distribution, and tracing particle trajectories.

If boundary conditions and space charge distribution are known, an electrostatic potential distribution in a closed space can be obtained from Poisson's equation. In the case of the analyzer examined here, there are very few spatial charges, and may be ignored in the normal design of the analyzer. Thus, the equation to be solved is reduced to Laplace's equation. Since the analyzer features an axisymmetric geometry, the problem is transformed into a two-dimensional problem through the use of a cylindrical-coordinate system, as follows.

$$\frac{1}{r}\frac{\partial \Phi}{\partial r} + \frac{\partial^2 \Phi}{\partial r^2} + \frac{\partial^2 \Phi}{\partial z^2} = 0 \quad (1)$$

In order to solve this numerically, the difference method is used; specifically, the Successive Over Relaxation (SOR) method, one type of relaxation method, is employed to carry out the iteration[26]. Taking grid points at the same intervals and converting the equation(1) to a difference equation, the electrostatic potential on the grid point (i, j) satisfies

$$\Phi_{i,j} = \frac{(\Phi_{i+1,j} + \Phi_{i,j+1} + \Phi_{i-1,j} + \Phi_{i,j-1})}{4} + \frac{(\Phi_{i+1,j} - \Phi_{i-1,j})}{8i} \quad (2)$$

By the SOR method, the present values are used to calculate new values, which are made to converge by iteration. From values of grid points at the k-th iteration, values at the (k+1)-th iteration can be obtained by the following equation.

$$\Phi_{i,j}^{(k+1)} = \omega(\tilde{\Phi}_{i,j}^{(k+1)} - \Phi_{i,j}^{(k)}) + \Phi_{i,j}^{(k)} \quad (3)$$

Here ω is a relaxation coefficient, which is specified in the range $1 < \omega$, and $\tilde{\Phi}_{i,j}^{(k+1)}$ is defined by the following.

$$\tilde{\Phi}_{i,j}^{(k+1)} = \frac{(\Phi_{i+1,j}^{(k)} + \Phi_{i,j+1}^{(k)} + \Phi_{i-1,j}^{(k+1)} + \Phi_{i,j-1}^{(k+1)})}{4} + \frac{(\Phi_{i+1,j}^{(k)} - \Phi_{i-1,j}^{(k+1)})}{8i} \quad (4)$$

After computation involving a few thousand iterations, variation of values in all grids nearly ceases.

Fig.4 shows examples of equipotential distributions obtained when electric potentials are applied to the electrodes. Parts to which electric potentials are applied are shaded in the figure. There are five control voltages: Vpu, Vpl, Vl, Vso, and Vsi. In the example of Fig.4, the upper electrode at the particle incidence component (Vpu) is set to 10 V, and the lower electrode (Vpl) of the same component is set to 0 V. Since it is generally cumbersome

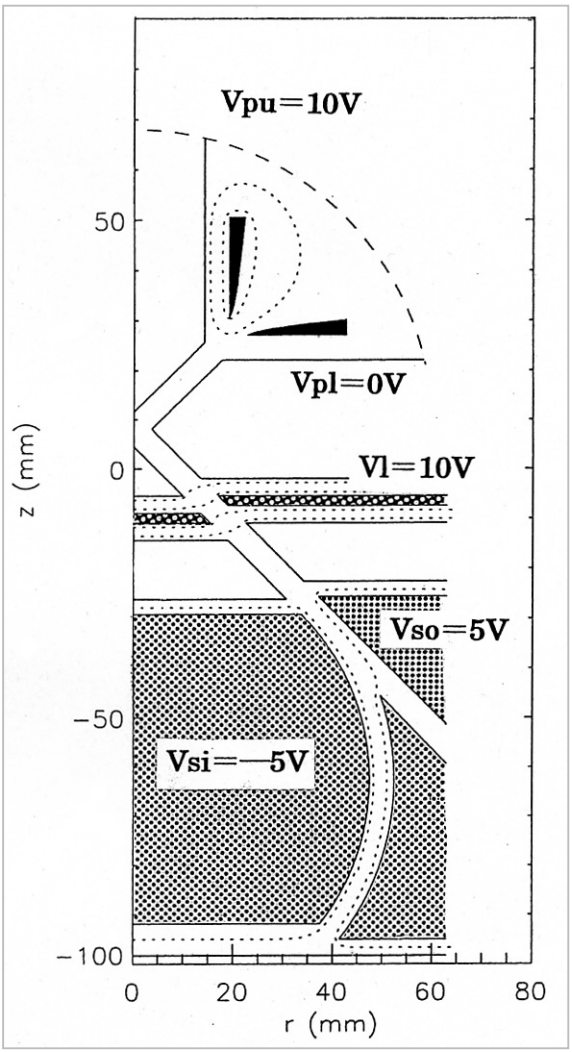

Fig.4 *Sensor configuration used for model calculation and an example of a solution for electrostatic potential distribution*

to reverse the polarity of a power supply, this analyzer is configured such that both Vpu and Vpl are specified as positive, and the electric field for deflection is formed by applying a positive voltage to one of the electrodes and applying a zero voltage to the other. The equipotential distribution shown in the figure is such that 10 V is also applied to the sensitivity adjusting electrodes (Vl). To the inner sphere (Vsi) and the outer sphere (Vso) of the spherical electrostatic analyzer, -5 V and +5 V are applied, respectively, based on the assumption that a positively charged ion is to be measured.

Two components of the electric field Er(r, z), Ez(r, z) are obtained from this potential distribution, and kinetic equations of the charged particle

$$\begin{cases} \dfrac{dv_r}{dt} = \dfrac{q}{m}Er + \dfrac{v_\theta^{\,2}}{r} \\ \dfrac{dv_\theta}{dt} = -\dfrac{v_r v_\theta}{r} \\ \dfrac{dv_z}{dt} = \dfrac{q}{m}Ez \end{cases}$$

are solved as initial value problems of an ordinary differential equation using difference method. Although the calculation is a two-dimensional problem until the inclusion of the electric field distribution, calculation of the particle trajectory becomes a three-dimensional problem. We examined the resolution and sensitivity of the analyzer by verifying the transmission (or non-transmission) to the exit (detector) of charged particles with various given conditions of incidence.

5 Results of Particle Trajectory Calculation

5.1 Characteristics of electrostatic incident-angle sweeper

An example of the particle trajectory at the electrostatic incident-angle sweeper component is shown in Fig.5. An electric potential featuring the same polarity as the incident particle is applied to one of the two electrodes of the incident-angle sweeping component. Here, the incident angle of the particle is defined by setting the direction of the symmetrical axis of the analyzer (z-direction in the cylindrical coordinate system) to 0˚ and setting the direction perpendicular to this to 90˚. Figures (a) and (c) on the left show examples in which particles with an incident angle of 15˚ are introduced into the analyzer; figures (b) and (d) on the right show examples in which particles with an incident angle of 75˚ are introduced into the analyzer. The two upper figures represent the r-z plane and the two lower figures represent a projection to the x-y plane.

The dashed line outside of the deflecting electrodes in Fig.5 (a) and (b) indicates a mesh to prevent the electric field from leaking outside of the instrument; the location of this mesh (at z = 0) is indicated with a dashed line in the figures below. The particles are made to enter the sensor from just outside of this mesh, in the leftward direction. Incident particles are arranged at intervals of 1 mm, with 12 in all, in the y-direction. Incident particles that reach the analyzer (i.e., particles that approach the origin in this figure) are represented by solid lines, while particles that hit the wall and cannot be transmitted are represented by dotted lines. The ratio of the electric potential applied to the deflecting electrodes to the energy of the incident particles here is 0.5. Because of the electrostatic structure, a proportionality relation is derived, with the results being interpreted as follows: in the case of (a), if the energy of the incident particle is 100 eV, then Vpu = 50 V; and if it is 2 keV, then Vpu = 1 kV.

In the plots in the r-z plane of Figs.5(a) and (b), the electrodes have an apparently symmetrical structure with respect to the 45˚ line, but three-dimensionally, the upper deflecting electrode is close to a cylinder and the lower deflecting electrode is close to a plane. For this reason, the formed potential structure acts as a convex mirror when electric potential is applied to the upper deflecting electrode, and acts as a concave mirror when

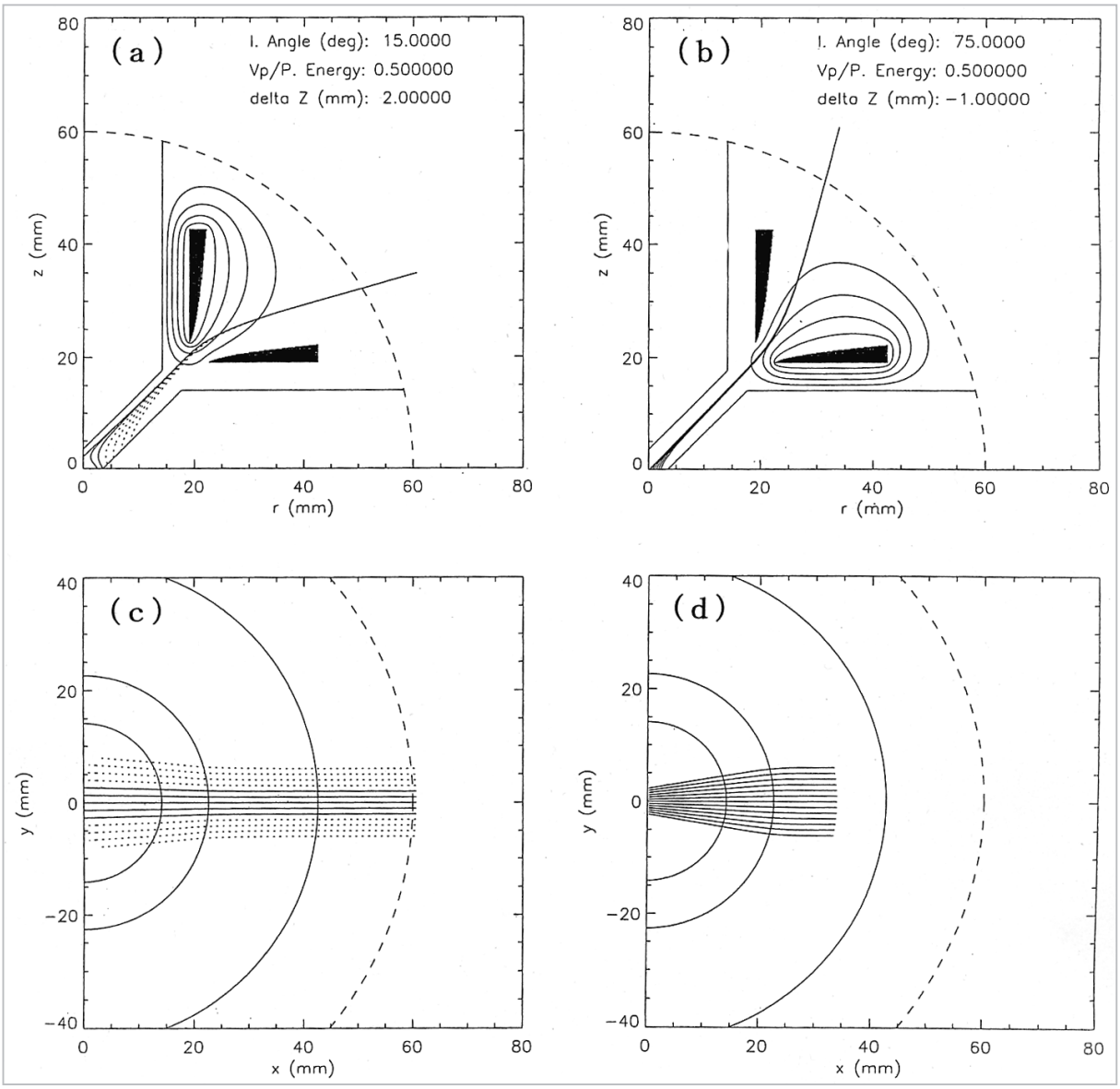

Fig.5 *Examples of particle trajectory in the electrostatic incident-angle sweeper component*

the electric potential is applied to the lower deflecting electrode. Therefore, the trajectories of parallel incident particles diverge in figure (c), and converge in figure (d). Because of this divergence/convergence effect, more particles with an incident angle of 75˚ are transmitted to the vicinity of the origin than particles with an incident angle of 15˚.

The relationships of incident angle to deflecting electrode voltage when three kinds of deflecting electrodes are adopted are shown in Figs.6 (a), (b), and (c). Figure (a) shows a case in which the deflecting electrode has the same shape and the same dimensions as those of Fig.4 and Fig.5. Here, multiple incident particles are located in the y-direction, as in the cases of Fig.5(c) and (d), and at the same time multiple incident particles are arranged in the direction (designated as Zp) perpendicular to both the initial trajectory of the incident particle and the y-direction; the number of transmitted particles is then investigated, and the results are displayed in contour representations. In other words, if the incident angle is 0˚, the Zp-direction coincides with the z-axis; if the incident angle is 90˚, it coincides with the x-axis. Now, since the particles are arranged at equal intervals, the number of transmitted particles is proportional to the effective aperture area of the analyzer. The

contour lines correspond to 0.05, 0.15, and 0.25 cm^2, from the outside to the inside, respectively. The Vp on the vertical axis indicates Vpu for incident angles less than 45˚, and Vpl for incident angles larger than 45˚. From this figure, it can be seen that both in cases where the electric potential is applied to the upper electrode and where it is applied to the lower electrode, the incident angle and the deflecting-electrode electric potential are nearly in proportion to each other. Moreover, it is confirmed that if an electric potential that is equivalent to the particle energy at the maximum is applied to the particle, a field of view from 0˚ to 90˚ can be covered. Furthermore, it can be seen that when electric potential is applied to the lower electrode (> 45˚), the deflection angle is large relative to a case in which the electric potential is applied to the upper electrode (< 45˚). It is believed that the effect of deflection varies depending on whether the potential structure is convergent or divergent; this would explain the difference between cases (c) and (d) of Fig.5. In addition, as can be seen in the comparison of (c) and (d) in Fig.5, due to the combination of divergence and convergence of the incident particles, particles with larger incident angles are transmitted through this electrostatic deflecting electrode component more easily.

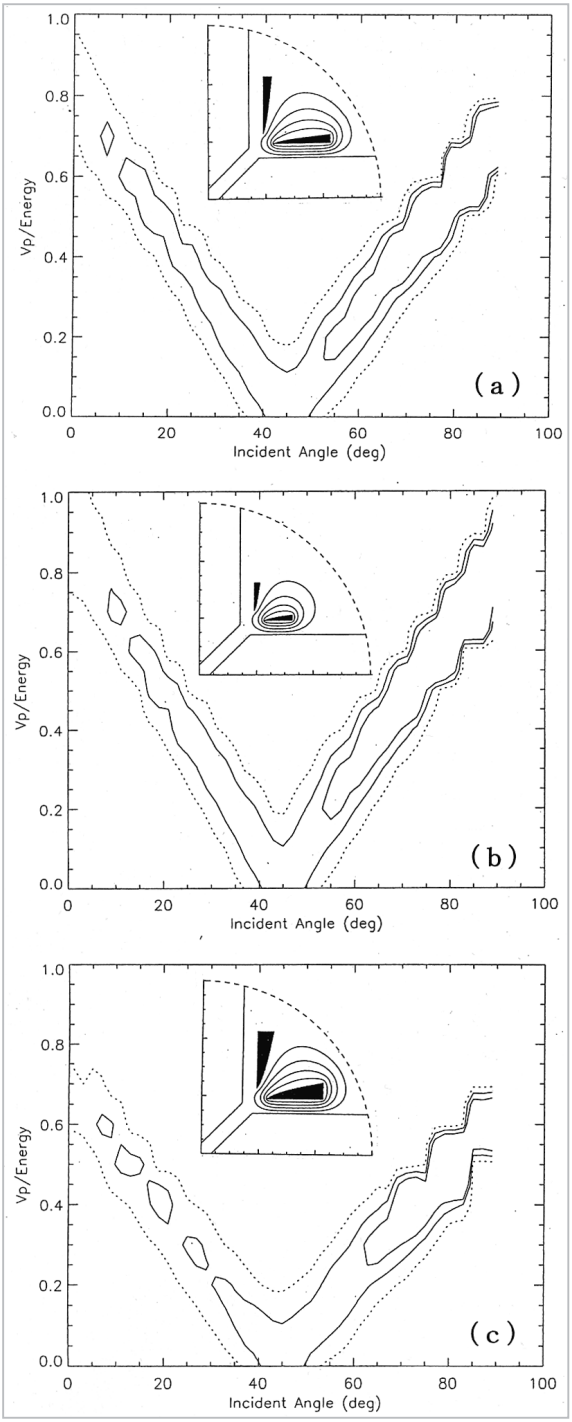

Fig.6 *Relationship between particle incident angle and deflecting-electrode voltage*

Next, cases in which the shape and dimensions of the deflecting electrodes are changed are shown in figures (b) and (c) of Fig. 6. Figure (b) shows a case in which the width of the electrode is reduced by half, and (c) shows a case in which the thickness of the electrode is increased. In the case of (b), where the deflecting electrode is made smaller, the voltage to be applied to the deflecting plates becomes larger. In other words, the effect of deflection has been reduced. This is because, due to the smaller size of the electrode, the space in which the potential is allowed to expand becomes reduced, and accordingly the spatial distribution of the electric field is also reduced. This is believed to be due to a reduction in the total effect of deflection resulting from a shortened range of integration, as the total effect of deflection is an integral effect of deflection along the trajectory. On the other hand, large deflection is attained in the case of (c). This is believed to be due to the increase in the electric field resulting from the increased thickness of the electrodes and the reduced spacing between the electrodes,

which causes the particle trajectory to bend to a larger degree. Thus, although some differences might arise depending on the shape and dimensions of the electrodes, it is possible to cover half of the celestial sphere within a field-of-view range of 0˚ to 90˚.

5.2 Energy-angle characteristics of analyzer

Next, the characteristics when a particle is measured all the way to an electrostatic analyzer will be examined. Fig.7 shows the trajectory of a particle with a 45˚ angle of incidence to a detector plane, in a case of deflection voltage of Vpu = Vpl = 0 V. As in the case shown in Fig.8, multiple incident particles are arranged in the y-direction, and particles that hit the wall halfway and cannot be transmitted to the detector surface are represented by dotted lines. A method of providing electric potentials to the inner sphere and the outer sphere of the analyzer in this case may be defined as Ko/(q·Vso) = -Ko/(q·Vsi) = 8.8, where Ko is particle energy and q is electric charge.

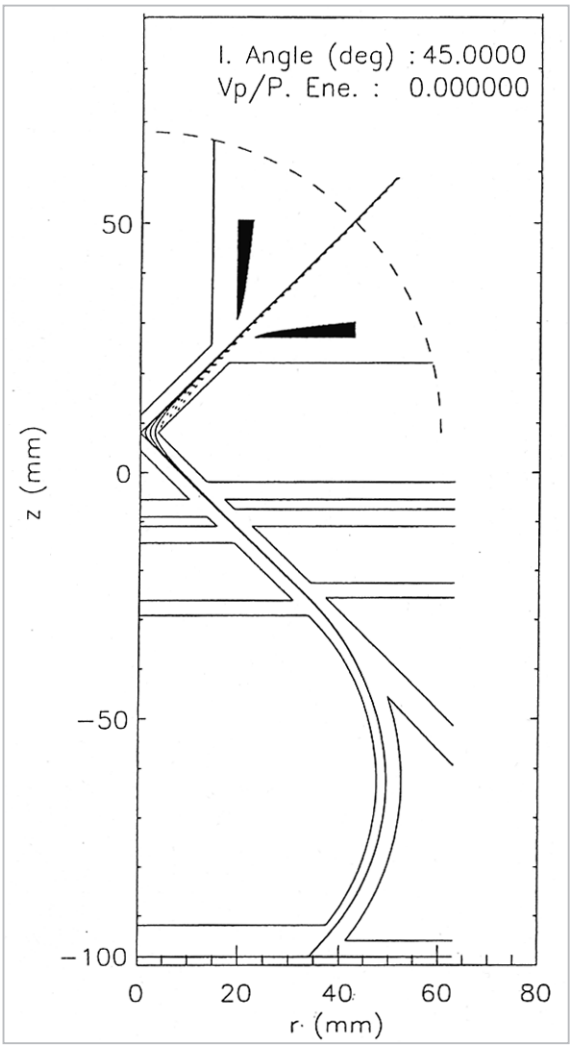

Fig.7 *Example of trajectory of a particle arriving at the detector plane*

Fig.8 shows a projection to the x-y plane of the particle trajectory in this case. The upper figure (a) of Fig.8 is for an incident angle of 45˚, and corresponds to Fig.7. As is characteristic of spherical analyzers, a beam of parallel incident particles has foci at points of the analyzer angles 90˚ and 270˚. Consequently, it will be possible to analyze the incident azimuthal angle of the particles ($\phi = \tan^{-1}(y/x)$) by arranging detectors with positional resolution at these points.

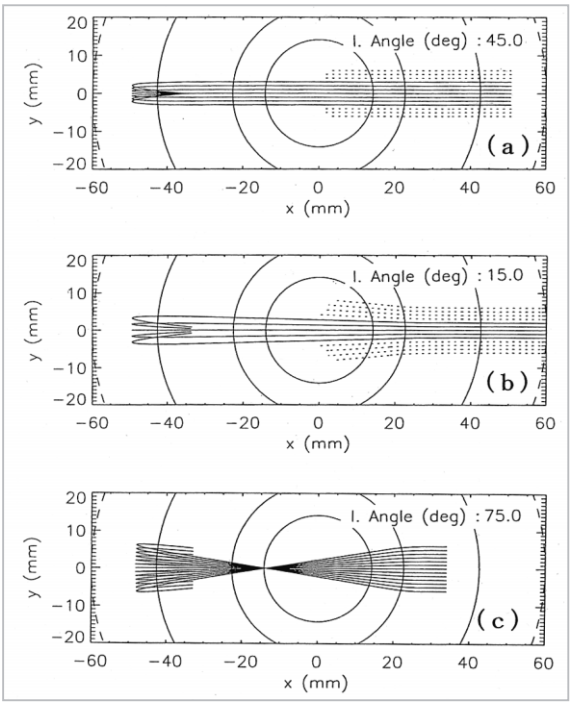

Fig.8 *x-y plane projection of particle trajectory*

Figures (b) and (c) show cases of incident angles of 15˚ and 75˚, respectively. As is already clear from Fig.5, the particle trajectory is bent, diverging in the case of the 15˚ angle and converging in the case of the 75˚ angle by the electrostatic deflecting electrodes following entry of the particle into the electrostatic analyzer. Therefore, in the case of (b), con-

vergence in the analyzer is insufficient, and the particle beam is not completely focused when it arrives at the detector plane. On the other hand, in the case of (c), a convergence point is located a considerable distance from the detector plane in the forward direction, and the particle beam is significantly widened when it arrives at the detector plane. This means that as the incident angle approaches 90˚, the resolution in the azimuthal-angle direction tends to decrease. However, in order to obtain significant angle resolution, it is necessary to multiply the obtained angle resolution by $\cos\alpha$, as a correction term for the incident angle (α). That is, for an incident angle of 90˚, the particles fall on the anodes. In this case, the azimuthal angle resolution is reduced to zero, but in this case 90˚ represents only one possible direction of the symmetric axis of the instrument; in this case there is no particular significance to the azimuthal angle.

The characteristics of the electrostatic analyzer are described as energy-angle characteristics. Fig.9 illustrates the relationship between the incident angle and energy characteristics for a case in which the electrostatic deflecting voltage is set to Vpu = Vpl = 0 V. The contour lines in the figure indicate effective aperture areas, as in the case of Fig.6, where the contour lines represent 75 %, 50 %, and 25 % of the peak value. The value of Vs used to scale the vertical axis is Vs = 2|q·Vso| = 2|q·Vsi|. From this figure, the incident angle of the center transmission with no deflecting voltage applied is seen to be 45˚, with a half-value width of about ±2˚. Note that although the half-value width determined from Fig.6 is larger than this value, Fig.6 shows the angular characteristic of the electrostatic deflecting component at the entrance only, while in Fig.9 the angular characteristic includes the analyzer in addition to the electrostatic deflecting component.

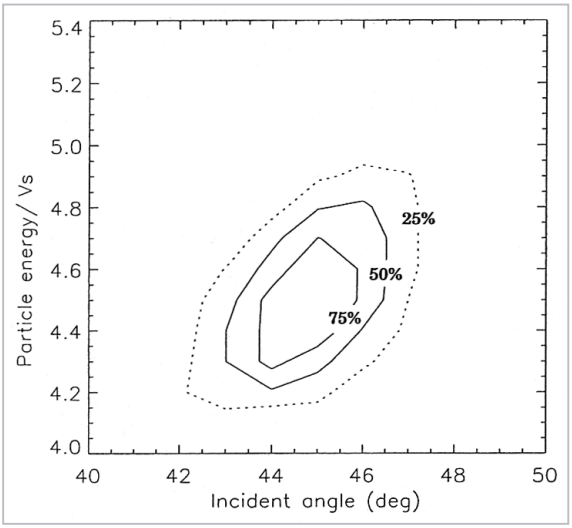

Fig.9 *Relationship between the energy and incident-angle characteristics for incident angles at or near 45˚*

In the case of the spherical electrostatic analyzer, since the electric potential is inversely proportional to the distance from the center of the concentric circles, the energy of a particle transmitted in a circular trajectory with a radius of 50 mm around the center of the inner and outer spheres is given by $Ko = q(VsoRo^2 - VsiRi^2)/(Ro^2 - Ri^2)$. The substitution Vso = -Vsi, Ri = 47.5 mm, and Ro = 52.5 mm in this equation gives Ko / (q·Vso) = 10.025. The result indicates that a particle having energy approximately 10 times that of the applied voltage can be measured. That is, with the use of a high-voltage power supply with a maximum output of ±3 kV, a particle having up to 30 keV/q will be measurable.

The above-mentioned Vs becomes half of 9.48, resulting in Ko/Vs = 4.74. It is believed that transmitted particles will possess energy near this value. In Fig.9, the center-transmission energy is approximately Ko/Vs = 4.5, which is in rough agreement with the above value, albeit slightly lower. We believe that this is because the electric field at the entrance of the spherical analyzer is lower than in the case of complete concentric spheres due to the optical trap attached at this position on the analyzer; as a result, the center transmission shifts to a slightly lower energy. Moreover, the half-value width here is approximately ±6%, and this value corresponds to the energy resolution of this analyzer.

The sensitivity of the particle measuring instrument is usually designated as the G ("Geometric") factor. Denoting the G factor by the symbol G, a relationship C (Ko) = (ε·

G·F (Ko) exists between the count rate per second (C) actually measured and the deferential flux of particle F (/cm^2 sec str eV). Here, ε is the detection efficiency of the detector and Ko is the energy of the measured particle. Now, G for an azimuthal angle of 1˚ in the detector plane is found to be 2.4×10^{-5}cm^2 str eV by integrating the results of Fig.9. Incidentally, if the anode of the detector on x-y plane has a spread of 3˚, the G factor will take a value three times larger than this value.

Fig.10 shows the relationship between the energy and incident-angle characteristics with the incident angle being deflected by the application of a voltage to the electrostatic deflecting electrodes. Four examples are shown in the figure; in each a constant deflecting voltage is applied. The figure shows that when the incident angle is deflected significantly away from 45˚, the width of the transmission angle is widened. In the case of (a), the half-value width is widened to approximately ±6˚; even in the case of (d), it reaches ±3˚. This means that the angle resolution is reduced at locations where the incident angle is significantly deflected. On the other hand, it turns out that the center transmission energy and its half-value width are nearly unchanged.

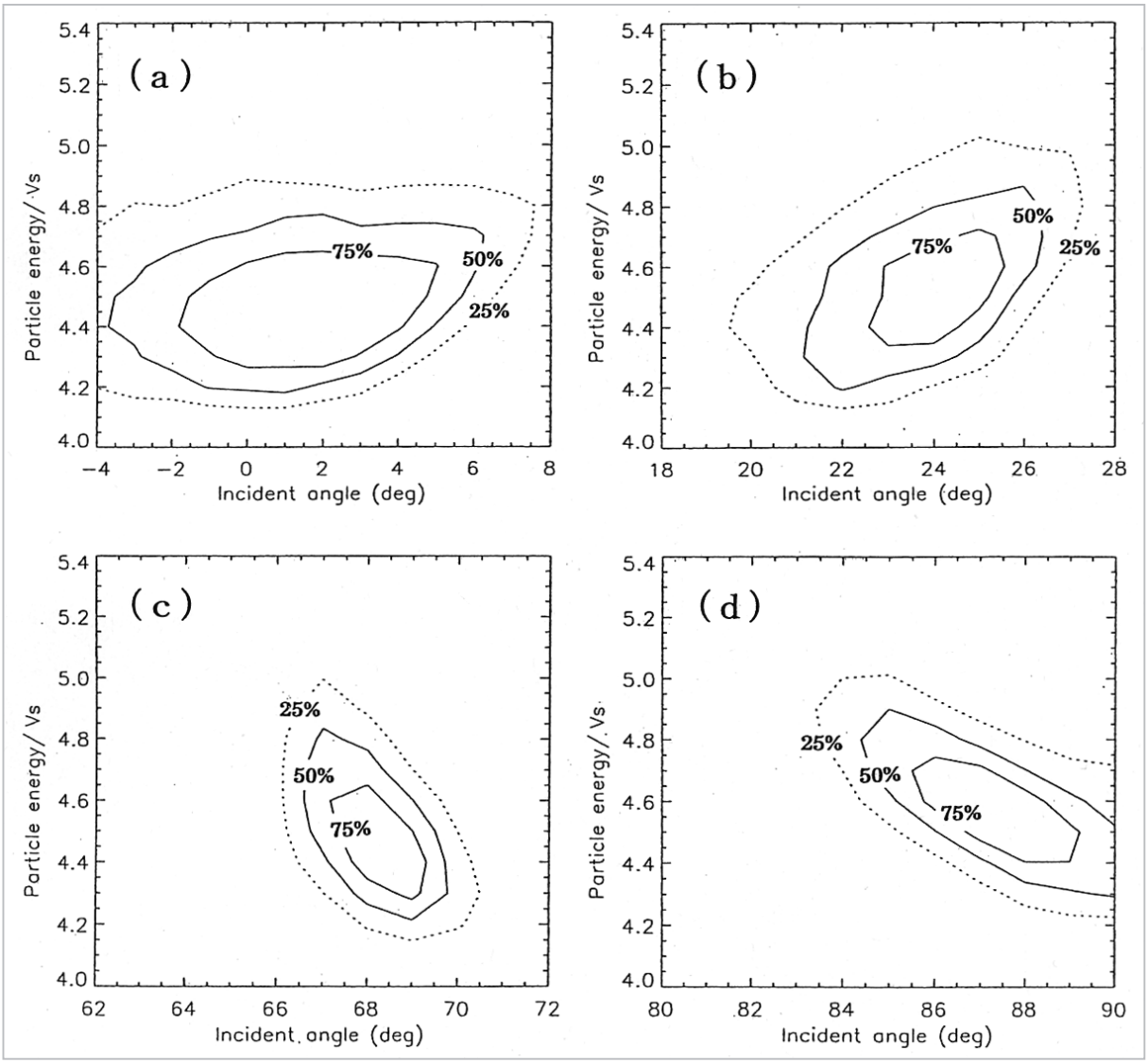

Fig.10 *Relationship between the energy and incident-angle characteristics when the incident angle is significantly deflected by a voltage applied to the electrostatic deflecting electrodes*

5.3 Sensitivity adjustment limiter characteristic

Fig.11 shows the transmission characteristics when the voltage of the sensitivity adjusting electrodes (Vl) is varied as a function of particle energy and incident angle. Figure (a) shows a case in which Vl = 4.4 Vs/q (where the definition of Vs is as described above) and (b) shows a case in which Vl = 4.6 Vs/q. In both cases Vpu = Vpl = 0 V. If the voltage of the sensitivity adjusting electrodes is 0 V, the transmission is reduced to the incident-angle distribution centered on 45˚(Fig.9). To facilitate comparison between Fig.9 and Fig.11, the values of the contour lines are shown using the peak value of Fig.9 as a reference value. The straight dashed line in the figure indicates the value of q·Vl. It is assumed that particles featuring energies larger than this value are capable of being transmitted. However, since the electric potential near the center of the analyzer path is slightly lower than Vl, the value should be considered for reference only.

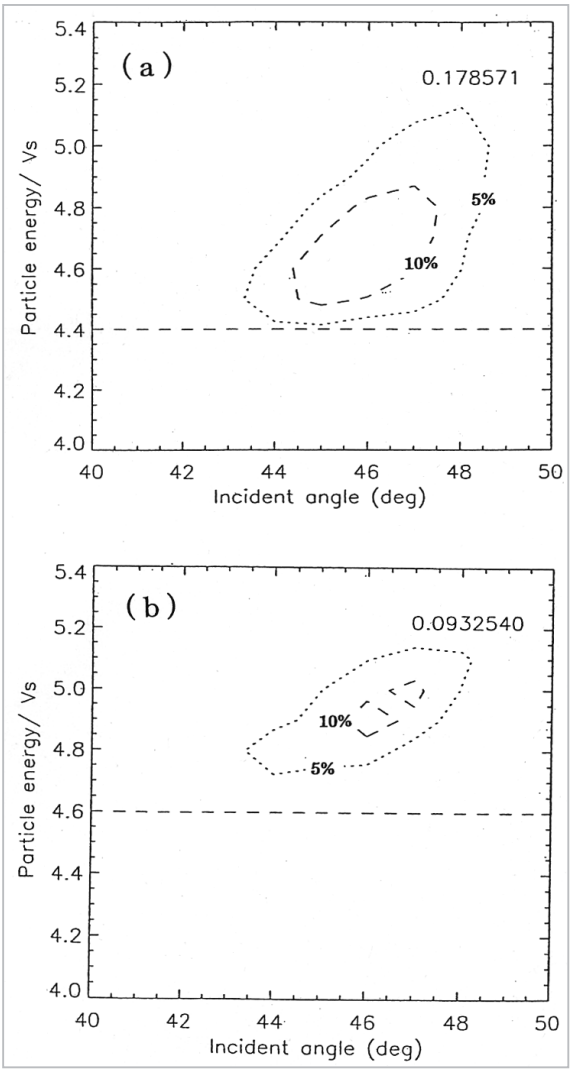

Fig.11 *Relationship between the energy and incident-angle characteristics when sensitivity adjustment limiter is in operation*

The number in the upper right of the figure indicates the integral value in this energy-angle plane divided by the integral value in the case of Vl = 0 V (Fig.9); the result is an indicator showing the extent to which sensitivity is masked with a "diaphragm." Thus, it follows that the sensitivity is adjusted to approximately 18 % for (a) and to approximately 9 % for (b). From these figures, it can be said that sensitivity adjustment within a range of approximately 10 % is entirely possible. However, it must be noted that the center transmission energy and the center incident angle tend to shift as the applied voltage Vl is increased. Moreover, in connection with this phenomenon, the half-value widths of the transmission energy and of the incident angle increase: the energy width reaches about ±2 % and the incident-angle width reaches about ±1.5˚ in the case of (b).

From careful comparison between Figs. 11(a), (b), and Fig. 9, it is found that the change seen from Fig. 9 to Fig.11 is not a simple one, insofar as the lower-energy portion (corresponding to the area below the dashed line in Fig.11) is disregarded in Fig.9; the number of high-energy particles positioned above the dashed line is also considerably decreased. These phenomena suggest that the electric field generated by Vl neither simply slows particles nor reflects them, but rather changes their trajectories by deflection, impeding transmission thereof both at and after the sensitivity adjusting electrodes.

To clarify the effects of this electrostatic sensitivity adjustment component on the particle trajectories, the initial spatial distribution of the incident particles and the spatial distribution of the finally transmitted particles on the detector plane are shown in Fig.12. Fig-

ures (a) and (b) show the initial and final distributions in the case where Vl = 0 V; i.e., when sensitivity adjustment is not applied. Figure (a) shows the initial distribution, with particles distributed in the y-Zp plane as explained in the description of Fig.6, at intervals of 1 mm in the y-direction and 1 mm in the Zp-direction. The diamonds represent the initial positions of particles that arrive at the detector plane while the dots represent those of particles that hit the wall halfway and cannot be transmitted. Final positions on the detector plane of the particles departing from the positions indicated by diamonds are shown in figure (b), with the beam of parallel incident particles focused at a point 90˚ from the analyzer, as described above with reference to Fig.8. Moreover, this point not only provides the focus in the y-direction (more specifically, in the azimuthal-angle direction) but also provides the focus in the x-direction (or in the r-direction). This feature is characteristic of the spherical electrostatic analyzer.

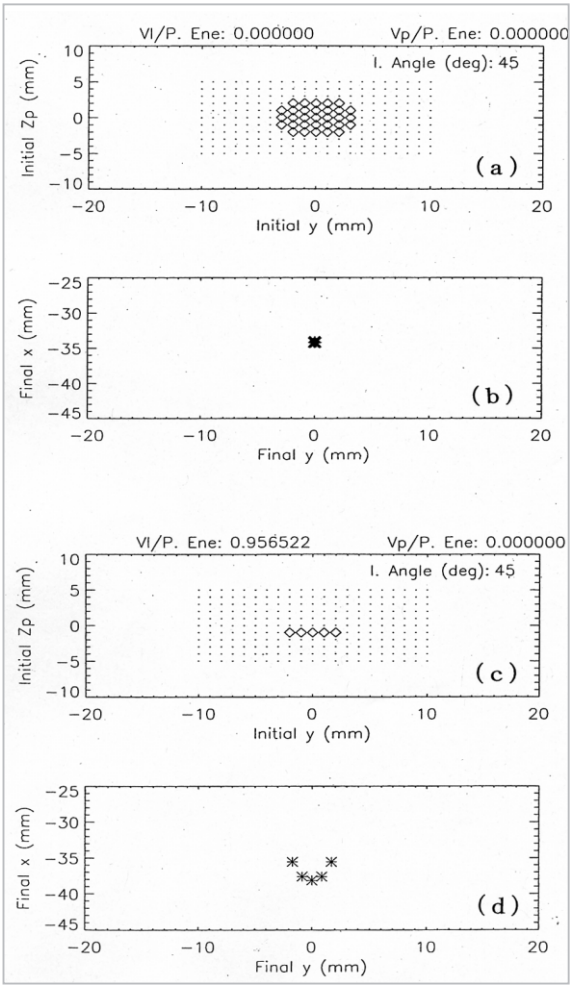

Fig.12 *The initial and final distributions of incident particles on the detector plane*

In contrast to the above case, figures (c) and (d) show the initial and final distributions in the case where a voltage Vl = 0.956 Ko/q is applied, where Ko is particle energy. Note that (c) is in the same format as (a), and (d) is in the same format as (b). In this case, the positions of the transmitted particles are limited to those represented by the diamonds shown in figure (c), and the final positions thereof on the detector plane are distributed as shown in figure (d). Here it is found that the trajectories are disturbed by the electric field of the sensitivity adjusting electrodes and that the focus of the 90˚ analyzer angle is blurred. This blurring corresponds to approximately ±3˚ or so in terms of the half-value width of the azimuthal angle distribution. As described above, meaningful resolution in practice is determined as a function of this value multiplied by cos α (α is the incident angle). For 45˚, the value becomes approximately ±2˚.

6 Summary and Discussion

Examination results using the numerical model for the measuring instrument in the foregoing examples are summarized as follows.

(1) With the electrostatic deflecting electrodes at the entrance, the incident angle can be deflected from 0˚ to 90˚ for particles having energies of up to approximately [maximum applicable voltage] × [quantity of electricity], and thereby half of the entire celestial sphere can be brought into the field of view.

(2) The center energy of particles that are transmitted through the electrostatic analyzer is roughly 9 q·Vso, the energy resolution is 12 %, and the resolution of the incident angle is almost 4˚ for an incident angle of 45˚. Moreover, the G factor for the incident particles of incident angles of 45˚ and its vicinity is 2.4×10^{-5} cm^2 str eV for a detector plane azimuthal-

angle width of 1˚.
(3) By applying a voltage of up to approximately [particle energy]/[quantity of electricity] on the electrostatic sensitivity controller, sensitivity control of up to approximately 10 % can easily be achieved, leading also to improved energy resolution and incident-angle resolution.
(4) On the other hand, when a voltage is applied to the electrostatic deflecting electrodes and the sensitivity control electrodes, it will affect the convergence of the particle beam in the spherical electrostatic analyzer, and hence resolution in the azimuthal-angle direction will vary.

We may conclude that for electron measurement in which a field of view covering almost the entire celestial sphere is desired, the use of two measuring instruments may be recommended. Moreover, the maximum output of a high-voltage power supply (several keV) serves as a rough limit to the inclusion of the entire celestial sphere in the field of view, and a distribution along a cone of a vertex of 45˚ can be obtained up to the maximum measurement energy. In the case of electrons, since distribution is expected to depend on only the pitch angle with respect to the magnetic field lines, all pitch angles can be covered if this conical surface is parallel to the magnetic field lines.

In the case of electrons, an angle resolution as wide as 4˚ to 10˚ or so and an energy resolution of approximately 12 % can be covered quite easily, and the temperature and anisotropy of the thermal electrons can be measured sufficiently. Moreover, Table 1 indicates that the number of electrons in the solar wind, or flux, approaches approximately 10^7 /cm^2 sec str eV. Assuming that the width of the anode used to measure the azimuthal angle distribution is 30˚, the G factor for an incident angle of 45˚ and thereabouts becomes 7.2×10^{-4} cm^2 str eV. The count determined based on this data approaches approximately 10^4 /sec. Total count for the entire surface of the detector is about 10^5 /sec.

The directions of arrival of the ions in the solar wind strongly converge in the solar direction (Fig.2). Because of this, it is not necessary to sweep half of the celestial sphere, from 0˚ to 90˚, using the electrostatic deflecting electrodes, but rather it is sufficient to sweep only the region near the Sun. On the other hand, in order to detect particles reflected and accelerated by the shock and also to detect the pickup ions, it is preferable to sweep a certain extent of the field-of-view angle. With this analyzer, when a high-voltage power source capable of a maximum output of 3 kV is used, the field-of-view angle for particles with energies equal or greater than 10 keV is limited to about 45˚ ±15˚ or less. Since information may be obtained for the 45˚ azimuthal angle along the conical surface, the sensor can cover a certain extent of the field-of-view angle.

As shown in Fig.2, the solar wind protons converge in the solar direction, with a narrow spread relative to the energy of the count peak. It can be said that for a set corresponding to an energy resolution of 12 % and an angle resolution of 4˚ for incident angles of 45˚ or thereabouts, a proton velocity distribution function may somehow be obtained. On the other hand, the proton energy flux reaches the order of approximately 10^8 /cm^2 sec str eV, as shown in Table 1. Therefore, from the G factor for the case in which one anode covers a width corresponding to an azimuthal angle of 1˚, a count on the order of approximately 10^4 /sec is expected. In reality, it is impractical to arrange anodes each with a width of 1˚; it is assumed that the lower-limit width is in fact 3˚ to 5˚ or so. Based on the angle spread of the solar wind protons, the total count on the whole surface of the detector reaches the order of 10^5/sec.

Regarding heavy ions in the solar wind, H^{++} yields counts one or more orders of magnitude lower than proton counts, and ions other than He^{++} yield counts two to three (or more) orders of magnitude lower than proton counts. These heavy ions strongly converge in the solar direction (Fig.2). Because of this, it can be said that although it is possible to iden-

tify He^{++} and other ions and to obtain the total flux for each ion (with energy and angle resolution corresponding to incident angles of 45° and the vicinity, it is difficult to obtain information for each velocity distribution function.

In the MCP used in the detector, the gain is reduced if the output current (namely, the count) becomes too large[27]. Although this saturation value depends on the resistance value of the MCP, a reference value of 10^6/sec. may be used in measurement. MCP life is also said to depend on the total amount of electric charge that has been emitted from the MCP[26]. Therefore, operations must involve the application of voltage to the sensitivity adjusting electrodes such that the count does not exceed 10^5/sec. In the present condition, it is estimated that the region of the proton peak corresponds to this state. Although the application of a voltage to the sensitivity adjusting electrodes will reduce the resolution in the azimuthal-angle direction (Fig.12), this is not of great consequence, as the reduced resolution is comparable to the resolution at the anode of the actual detector. It is hoped that such application of a voltage will enhance energy resolution (Fig.11), which will provide for finer observation of the proton energy distribution.

From our investigation to this point, we have concluded that despite given limits, the sensor can be expected to cover measurement targets sufficiently. Particularly in terms of electron measurement, we may safely conclude that there are no problems with the current design. One of the remaining problems lies in the maximum measurement energy for ions, which is currently limited to about 30 keV/q. For measurement allowing this limit to be extended to 60 keV/q or so, a method may be employed in which the radius of the spherical electrostatic analyzer is enlarged while particle path spacing is maintained at the present value of 5 mm. Incidentally, if the inner sphere radius and the outer sphere radius are enlarged to 87.5 mm and 92.5 mm, respectively, measurement of energies as high as approximately 60 keV/q will be possible with a high voltage of ±3 kV. However, this raises the problem of enlargement of the overall measuring instrument. In addition, another issue that remains to be addressed in the measurement of ions is the investigation of a function for selection of mass using the TOF method.

7 Concluding remarks

Through this research, we have investigated the basic prospect of realizing solar wind ion and electron measurement with a satellite employing three-axis control. When NASA's LWS program[28] establishes observation points for investigation of solar wind plasma across a vast region of space in the vicinity of the Earth (including the L5 point), the co-rotating high-speed solar wind, shock and disturbance accompanying CMEs, and the propagation of related phenomena will all be observable within a multiple-point system. It is hoped that this measurement, combined with imaging observation data in the vicinity of the Sun, will greatly enhance our understanding of spatial structures and the propagation of solar wind disturbances, as well as deepen our understanding of the generation and propagation of high-energy particles and the like, which will in turn lead to improved space weather forecasting. Hopes are high that the solar wind plasma measurement of the L5 mission will play a part in the further exploration of space weather applications.

References

1 M. Akioka, "L5 Mission and Observation of Interplanetary CME", This Special Issue of CRL Journal.

2 B. T. Tsururani and W. D. Gonzarez, "The interplanetary causes of magnetic storms: a review", in 'Magnetic Storms', Geophysical Monograph, Vol. 98, 77, 1997.

3 S. J. Bame J. R. Asbridghe, W. C. Feldman, J. T. Gosling and R. D. Zwickl, "Bi-directional streaming of electrons 80 eV: ISEE evidence for a closed-field structure within the driver gas of an interplanetary shock", Geophys. Res Lett., Vol. 8, 173, 1981.

4 J. T. Gosling, D. N. Baker, S. J. Bame, W. C. Feldman and R. D. Zwickl, "Bi-directional solar wind electron heat flux events", J. Geophys. Res., Vol. 92, 8519, 1987.

5 S. Watari and T. Denton, "In situ local shock speed and transit shock speed", Ann. Geophys., Vol. 16, 370, 1998.

6 N. Golpalswamy, A. Lara, P. Lepping, M. L. Kaiser, D. Berdichevsky, and O. C. St. Cyr, "Interplanetary acceleration of coronal mass ejections", Geophys. Res. Lett., Vol. 27, 145, 2000.

7 B. T. Tsurutani, W. D. Gonzarez, F. Tang, S. I. Akasofu, and E. J. Smith, "Origin of interplanetary southward magnetic fields responsible for major magnetic storms near solar maximum (1978-1979)", J. Geophys. Res., Vol. 93, 8519, 1988.

8 D. V. Reames, "Particle acceleration at the sun and in the heliosphere", Space Sci. Rev., Vol. 90, 413, 1999.

9 G. Gloeckler, L. A. Fisk, T. H. Zurbuchen and N. A. Schwadron, "Sources, injection and acceleration of heliospheric ion populations", in 'Acceleration and transport of energetic particles observed in the heliosphere: ACE 2000 symposium', 221, 2000.

10 L. A. Fisk, G. Gloeckler, T. H. Zurbuchen and N. A. Schwadron, "Ubiquitos statistical acceleration in the solar wind", in 'Acceleration and transport of energetic particles observed in the heliosphere: ACE 2000 symposium', 229, 2000.

11 T. H. Zurbuchen, L. A. Fisk, N. A. Schwadron and G. Gloeckler, "Observations of non-thermal properties of heavy ions in the solar wind", in 'Acceleration and transport of energetic particles observed in the heliosphere: ACE 2000 symposium', 215, 2000.

12 G. Gloeckler and J. Geiss, "Interstellar and inner source pickup ions observed with SWICS on ULYSSES", Space Sci. Rev., Vol. 86, 127, 1998.

13 H. Fichtner, "Anomalous cosmic rays: messengers from the outer heliosphere", Space Sci. Rev., Vol 95, 639, 2001.

14 R. von Steiger, J. Geiss and G. Gloeckler, "Composition of the solar wind", in 'Cosmic winds and the heliosphere', 581, 1997.

15 G. Gloeckler. L. A. Fisk, S. Hefti, N. A. Schwadron, T. H. Zurbuchen, F. K. Ipavich, J. Geiss, P. Bochsler and R. F. Wimmer-Schweingruber, "Unusual composition of the solar wind in the 2-3 May 1998 CME observed with SWIDS on ACE", Geophys. Res. Lett., Vol. 26, 157,1999.

16 R. M. Skoug, S. J. Bame, W. C. Feldman, J. T. Gosling, D. J. McComas, J. T. Steinberg, R. L. Tokar, P. Riley, L. F. Burlaga, N. F. Ness and C. W. Smith, "A prolonged He^{+} enhancement within a coronal mass ejection in the solar wind", Geophys. Res. Lett., Vol. 26, 161, 1999.

17 S. Shodhan, N. U. Crooker, S. W. Kahler, R. J. Fitzenreiter, D. E. Larson, R. P. Lepping, G. L. Siscoe, and J. T. Gosling, "Counterstreaming electrons in magnetic clouds", J. Geophys. Res., Vol. 105, 27261, 2000.

18 R. P. Lin, "WIND observations of suprathermal electrons in the interplanetary medium", Space Sci. Rev., Vol. 86, 61, 1998.

19 R. E. Ergun, D. Larson, R. P. Lin, J. P. McFadden, C. W. Carlson, K. A. Anderson, L. Muschiette, M. McCarthy, G. Parks, H. Reme, J. M. Bosqued, C. d'Uston, T. R. Sanderson, K. P. Wenzel, M. Kaiser, R. P.

Lepping, S. D. Balle, P. Kellog and J. L. Bougeret, "Wind spacecraft observations of solar impulsive electron events associated with solar type Ⅲ radio bursts", Astrophys. J., Vol. 503, 435, 1998.

20 N. Shimada, T. Terasawa, M. Hoshino, T. Naito, H. Matsui, T. Koi, K. Maezawa and the GEOTAIL/LEP/MGF/HEP teams, "Diffusive shock acceleration of electrons at an interplanetary shock observed on 21 Feb. 1994", Astroph. Space Sci., Vol 264, 481, 1999.

21 T. Mukai, W. Miyake, T. Terasawa and K. Hirao, "Observations of solar wind ions by the interplanetary spacecraft Suisei (Planet-A)", J. Geomag. Geoelectrc., Vol. 39, 377, 1987.

22 G. Borrini, J. T. Gosling, S. J. Bame and W. C. Feldman, "Helium abundance enhancements in the solar wind", J. Geophys. Res., Vol. 87, 7370, 1982.

23 W. C. Feldman and E. Marsch, "Kinetic phenomena in the solar wind", in 'Cosmic winds and the heliosphere', 617, 1997.

24 T. Mukai, S. Machida, Y. Saito, M. Hirahara, T. Terasawa, N. Kaya, T. Obara, M. Ejiri and A. Nishida, "The low energy particle (LEP) experiment onboard the GEOTAIL satellite", J. Geomag. Geoelectrc., Vol. 46, 669, 1994.

25 S. Machida, Y. Saito, Y. Ito and H. Hayakawa, "Instrument characteristics of the electron spectrum analyzer (ESA) onboard the Planet-B mission and observational perspectives of the electron measurements", Earth Planets Space, Vol. 50, 207, 1998.

26 H. Togawa, "Numerical calculations and simulations", Kyoritu Pub., 211, 1976. (in Japanese)

27 Technical report of MCP assembly, Hamamatsu Phtonics Co., 1991. (in Japanese)

28 http://lws.gsfc.nasa.gov/.

***MIYAKE Wataru**, Dr. Sci.*
Senior Researcher, Space Weather Group, Applied Research and Standards Division
Space Weather

***KAZAMA Youichi**, Ph. D.*
Swedish Institute of Space Physics
Space Plasma Physics